Crossflow Transition on a Pitched Cone at Mach 8

Joshua B. Edelman*, Katya M. Casper†, John F. Henfling‡, Russell W. Spillers§
Sandia National Laboratories, Albuquerque, NM, USA,
Steven P. Schneider¶
School of Aeronautics and Astronautics, Purdue University, West Lafayette, IN, USA

Boundary-layer transition was measured on a pitched, 7° half-angle cone in a Mach 8 conventional wind tunnel. On a smooth cone, transition via second-mode waves was observed at all angles of attack. In addition, naturally-excited stationary crossflow waves were apparent in temperature sensitive paint images, but did not appear to lead to transition. Two patterns of roughness elements were used to generate higher-amplitude stationary crossflow waves. Breakdown of the stationary waves was observed. The roughness resulted in instability amplitudes nearly an order of magnitude larger than the smooth cone at the same Reynolds numbers and higher instability growth rates. Transition occurred 30% - 40% sooner using the roughness elements with peak amplitudes near 15 - 20%, for $\alpha \geq 4°$. A low-frequency, coherent wave was measured at all angles of attack. The calculated phase velocity shows a strong dependence on angle of attack, but the propagation angle is similar for all non-zero α. The measured wave properties do not agree with computations of the travelling crossflow wave, but are curiously similar to measurements of a suspected tunnel-noise-driven instability made on an elliptic cone at Mach 6.

Nomenclature

f	frequency, Hz	Re_∞	freestream unit Reynolds number
k	roughness height, mm or mils	T	temperature, K
m	wavenumber	U	velocity, m/s
M	Mach number	x	axial distance from nosetip, mm
p	pressure, Pa	α	angle of attack, deg
Re	Reynolds number based on axial distance from nosetip	δ	boundary layer thickness, based on 99.5% edge enthalpy, mm
Re_k	roughness Reynolds number, based on roughness height k, and conditions at k in the undisturbed boundary layer	θ	azimuthal angle from windward ray, deg

Subscripts		*Abbreviations*	
0	stagnation condition	HWT	Sandia National Laboratories Hypersonic Wind Tunnel
e	boundary layer edge condition		
∞	freestream condition		

I. Introduction

The state of the boundary layer — laminar or turbulent — can have direct effects on aerodynamic and heating loads. Understanding and predicting boundary layer transition is critical to the cost-effective and

*Graduate Student – Purdue University, Graduate Intern – Sandia National Laboratories, Student Member AIAA
†Senior Member of the Technical Staff, Engineering Sciences Center, Senior Member AIAA
‡Distinguished Technologist, Member AIAA
§Principal Technologist
¶Professor, Associate Fellow AIAA

safe design of hypersonic vehicles. A number of mechanisms can be responsible for hypersonic boundary layer transition on a vehicle, depending on its geometry and orientation, including the second mode and the crossflow instability.

For three-dimensional flowfields such as non-axisymmetric bodies and cones at an angle of attack, the crossflow instability can be important to transition away from the wind and lee rays. This instability results from a pressure gradient affecting the slower-moving fluid near the wall more than the outer fluid, generating a transverse component of the boundary layer flow. In the case of a cone at an angle of attack, the pressure is higher at the windward ray than the leeward ray, driving a crossflow around the cone from wind to lee. The crossflow component of the boundary layer is inflectional and therefore unstable. The crossflow instability can manifest as either stationary or travelling vortices.[1] Figure 1 illustrates the coordinate system for a cone at an angle of attack, and the notional paths of stationary crossflow vortices.

In environments with high freestream-noise, such as conventional wind tunnels, the travelling waves dominate transition at low speeds while stationary waves are important for low-freestream-noise environments.[2] This may not be generally true for hypersonic flow. Recent measurements by Borg et al. on an elliptic cone in noisy flow show that travelling waves may not be present at Mach 6.[3,4] Instead, there appears to be a tunnel-noise-driven low-frequency instability, with wave angles between 50–60° and phase speeds from 200–400 m/s. These results remain unclear and more work is needed to understand the nature of the measured instability.

Because flight environments are expected to have low freestream noise, most crossflow work has focused on stationary wave transition. Thorough reviews of crossflow transition experiments and computations up to the year 2003 are provided by Bippes[5] and Saric, et al.[1] Work on stationary crossflow wave transition, especially at high speeds, has continued in the years since. Of particular interest are the secondary instabilities which are generated by the large velocity gradients created by the stationary vortices. These have been well studied for low-speed flows mostly on swept wings,[6–9] and are beginning to be observed and computed at high speeds on sharp cones.[10–13] However, due to the influence of freestream noise on crossflow transition, most of the research on hypersonic stationary wave breakdown is limited to the few currently available quiet tunnels. At low speeds, a transition correlation based on N-factors of the secondary instabilities (around $N = 6 - 10$.) yields better results than correlations based on the stationary crossflow wave growth alone.[8] If this remains true at hypersonic speeds, then it would be beneficial to have the capability to study stationary crossflow waves in conventional, noisy tunnels.

Stationary crossflow waves are thought to be generated by surface roughness.[5] Thus even in a high-noise environment, suitably large roughness elements may result in large stationary waves which ultimately lead to transition. The observation of stationary waves in conventional, noisy hypersonic wind tunnels is not new. See, for instance, Section 5 of Reference 14. However, hypersonic stationary-wave dominated breakdown has mostly been studied in quiet tunnels. A few notable exceptions are IR thermography images and high-frequency pressure measurements by Muñoz et al.[15] and Kroonenberg et al.,[16] and temperature sensitive paint images by Swanson and Schneider,[17] all at Mach 6 in noisy tunnels. Given that stationary waves are expected to be the most important path to transition in crossflow-dominated regions of flight vehicles, a method to induce stationary-wave transition in any conventional tunnel would be a boon to hypersonic crossflow-transition research.

However, in some cases travelling waves may be relevant to transition. As pointed out by Li et al.,[18] if stationary wave initial amplitudes are low, such as for a polished surface, travelling waves may dominate due to their higher growth rates, even for low freestream noise. In addition, travelling waves and stationary waves can interact nonlinearly depending on their respective initial amplitudes.[19] Therefore even if travelling waves are not ultimately responsible for laminar–turbulent transition, they may have an effect on stationary wave growth and breakdown.

Travelling wave transition, including the development of secondary instabilities, has been studied in depth computationally, for both low and high speeds.[18,20–23] Several experiments measuring travelling waves have also been conducted.[24,25] At hypersonic speeds, travelling waves have been observed on both circular and elliptical cones. Poggie et al.[26] measured travelling waves on a 2:1 elliptic cone at Mach 8, at a freestream unit Reynolds number of 2×10^6 /m. They found waves at around 10-20 kHz as expected, but only achieved rough agreement with computations for the travelling wave properties. Borg et al.[3,27] measured travelling waves from very low amplitudes to transition on a 2:1 elliptic cone at Mach 6 in quiet flow. They achieved much better agreement with computations of the wave properties.[23] However, in noisy flow, no travelling crossflow waves were evident in the measurements. Bicoherence calculations and the lack of measured

harmonics indicate that travelling waves were not responsible for transition in either noise environment.

Muñoz et al.[15,28] measured travelling waves and the second mode on 7° and 15° half-angle circular cones at 6° angle of attack and Mach 6 in a conventional tunnel. For the 7° cone, the second mode appears to be responsible for transition. On the 15° cone, however, travelling crossflow appeared to be dominant near the 90° ray.

Ward[29] measured travelling waves and their properties on a 7° half-angle circular cone at 6° angle of attack at Mach 6, for both noisy and quiet flow. It is believed that the travelling waves were responsible for transition in noisy flow, though no harmonics or secondary instabilities are evident and the bicoherence was not calculated. However, the work of Wasserman and Kloker[20] and Li et al.[18] shows that the travelling wave secondary instabilities will appear as multiple frequencies in a stationary reference frame (i.e. a surface sensor), and these frequencies may overlap with the travelling wave frequencies. Therefore travelling wave secondary instabilities may not be easily identified from experimental measurements.

The present work seeks to extend measurements of crossflow-dominated transition in noisy hypersonic tunnels. Experiments were conducted on a 7 degree half-angle cone angles of attack between 0° and 8° in the Mach 8 Hypersonic Wind Tunnel at Sandia National Laboratories. Using small roughness elements near the nose of the cone, large stationary crossflow waves were generated and their breakdown was studied using surface pressure sensors and temperature sensitive paint. The experiments also investigated a low-frequency, travelling instability.

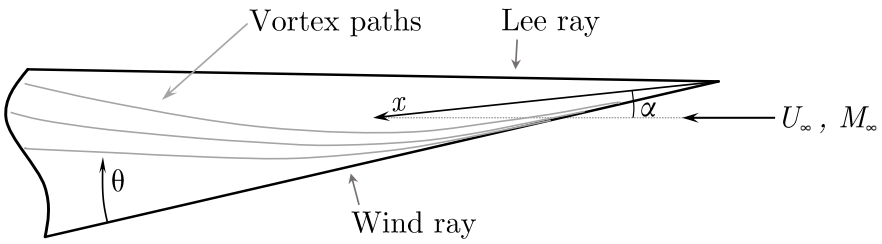

Figure 1. Schematic showing the coordinate system of the pitched cone.

II. Facilities and Instrumentation

II.A. Sandia National Laboratories Hypersonic Wind Tunnnel (HWT)

The experiment was conducted in the Sandia National Laboratories Hypersonic Wind Tunnel (HWT) facility. The HWT is a cold-flow, blowdown-to-vacuum wind tunnel with three interchangeable nozzles for Mach 5, 8, and 14. Mach 5 uses air as the test gas while Mach 8 and 14 use nitrogen. At Mach 8, the facility can reach a maximum unit Reynolds number of about 17.4×10^6 /m. The HWT stagnation temperature T_0 can be varied from 550 K to 890 K, and the stagnation pressure p_0 is chosen between 1700 kPa and 5500 kPa. The HWT is a conventional wind tunnel with freestream noise levels between 3 - 5% at Mach 8.[30] The test section has a diameter of 0.359 m. For the present work, the model was started at approximately 0° angle of attack, and pitched to $-8°$ in 2° increments. During model installation, the cone was leveled to within 0.01° using a precision bubble level. The maximum standard deviation of the angles of attack was 0.06°.

For the results presented here, the stagnation temperature was held roughly constant. The mean T_0 was 660 K, with a standard deviation of 45 K for all the runs. This resulted in a mean wall to edge temperature ratio $T_w/T_e = 3.5 \pm 0.3$. The freestream unit Reynolds number was calculated using the linear viscosity law $\mu = 6.8663 \times 10^{-8}\, T_\infty$, with freestream temperature T_∞ in K and viscosity μ in Pa·s.

II.B. Model and Instrumentation

The model used for these experiments was the Modular cone. This model has been used in previous experiments at Purdue University.[13,31] The Modular cone is a 7-degree half-angle, sharp, circular cone. It is 0.4 m long with a base diameter of 0.1 m (3.92 in). The nosetip has a radius of about 80 μm. The cone allows for

the use of interchangeable sensor frusta, each of which can be rotated to a specified orientation and locked into place prior to a run.

A roughness insert can be placed near the tip of the cone, with roughness elements at $x = 50.8$ mm. Several inserts have been fabricated with different roughness element heights and wavenumbers. The individual roughness elements are of the Chynoweth RIM design,[32] which are small cylindrical rods embedded into the insert. Table 1 provides the properties of the roughness inserts used in the present study. Figure 2 shows the placement of the roughness elements with respect to the sensor locations. The roughness elements spanned up to the 90° ray on the sensor side of the model. Note that for each insert the wind ray cuts between two elements, and 2 elements were placed on the non-sensor side of the model.

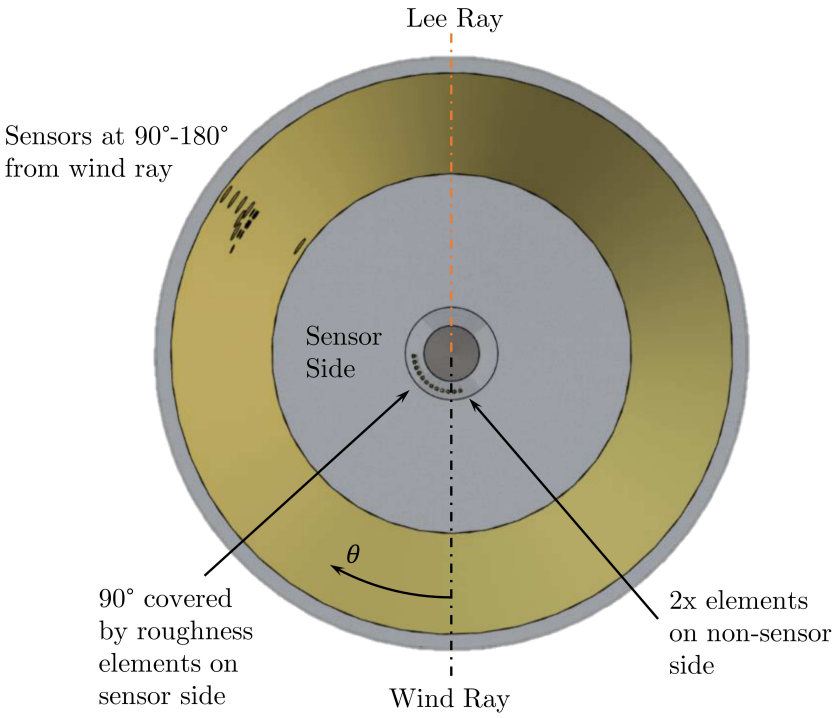

Figure 2. Diagram showing the roughness element placement with respect to the sensors. Flow is into the page.

A US3D CFD model was created for the 2°-8° angle of attack cases at $Re_\infty = 5.6\times10^6$ /m calculated using a linear viscosity law. To verify that the roughness was small enough that it only excited stationary waves but did not directly affect transition, its critical Re_k was calculated from the CFD data. The "critical" roughness size is defined as the size at which the roughness begins to affect transition (see Figure 1 in Schneider[33]). At 8° angle of attack and $Re_\infty \approx 6.2 \times 10^6$ /m, the Re_k upper bound for the 5 mil roughness elements is $Re_k \approx 60$. Note that the boundary layer thickens leeward, so the maximum Re_k is on the wind ray. According to Figure 18 in Schneider[33] (redrawn from Braslow[34]), on a flat plate at Mach numbers $M > 6$, the square-root of the critical roughness is $Re_k^{1/2} > 100$. The maximum Re_k in the experiment is below this critical value, so it is believed that the roughness does not directly cause transition.

The roughness height as a percentage of the boundary layer thickness at the roughness location ($x = 50.8$ mm), and the maximum Re_k at $Re_\infty = 6.2 \times 10^6$ /m is provided in Table 2. Note that the maximum ratio k/δ occurs at the wind ray.

II.C. Temperature Sensitive Paint

Temperature sensitive paint (TSP) using the Ru(bpy) luminophore was applied to the model. This is the same formulation as the TSP used at Purdue University.[13,31] Two LaVision Imager sCMOS cameras were used: one to capture the lee-side of the cone and the other centered on the 90° ray. The TSP was excited using two 400-nm ISSI water-cooled LED arrays, one for each camera. A long-pass filter was used to block

Table 1. Properties of the roughness elements used in the present study.

Roughness Insert	Num. Elements	k, mils	Diam., mils	m (spacing)
Smooth	-	-	-	-
RIM 12x-5	12	5	22	40, (9°)
RIM 7x-5	7	5	30	20, (18°)

Table 2. Ratios of k/δ for the two highest angles of attack.

α, deg.	Re_k	max k/δ	
		$Re_\infty = 5.6 \times 10^6$ /m	$Re_\infty = 12 \times 10^6$ /m
6	42	35%	53%
8	61	42%	61%

excitation light at each camera. The LaVision DaVis software was used to capture the images. Both cameras were run with 2 x 2 software binning. Details of the TSP reduction process can be found in Ward.[29] Table 3 provides details on the setup for each camera used.

Table 3. TSP camera setup specifications.

Orientation	Filter	Focal Length	Approx. Distance from Centerline
Lee-side	580 nm longpass	50 mm	0.71 m
90° ray-side	550 nm longpass	60 mm	0.64 m

II.D. Data Acquisition and Reduction

For the present work, a new sensor frustum was used with several closely spaced Kulite XCQ-062-15A and PCB132A31 pressure transducers. A type-T thermocouple on the surface of a MedTherm 8-1-0.25-48-20835TBS Schmidt-Boelter gauge was used to measure the model surface temperature. A schematic showing the sensor array is provided in Figure 3. In this paper, data from two PCBs are presented. These are labeled as PCB 9 (upstream) and 11 (downstream) in the schematic.

PCB data was sampled at 2.5 MHz and anti-aliasing filtered with a Krohn-hite 3944 4-pole low-pass Bessel filter at 1 MHz. Kulite data was sampled at 1 MHz and filtered at 400 kHz. The PCB132 sensors are high-pass filtered at 11 kHz, with a resonant frequency greater than 1 MHz.[35] The Kulite sensors have a resonance around 200-300 kHz. Power spectra and other spectral quantities were calculated using a frequency resolution of 1.25 kHz and a Hanning window with 50% overlap. Two seconds of data for each angle of attack was collected during a single run at a roughly constant unit Reynolds number.

Unless otherwise specified, the PCB data were taken at $x = 343$ mm and 123° from the wind ray. The power spectral densities (PSDs) of the PCB signals are normalized by the edge pressure at the PCB location taken from the US3D simulation, scaled by each run's freestream pressure. The amplitudes were calculated by taking the square-root of the integral under the PSD over the specified frequency range.

III. Stationary Crossflow Results

First, results are presented from the $\alpha = 6°$, baseline smooth-cone case in Section III.A. This is to provide a reference for natural transition on the cone. Patterned, discrete roughness elements were added near the cone nosetip to excite stationary crossflow waves. Measurements of transition with this roughness are presented in Section III.B. Finally, results from the smooth cone and with each roughness insert at each angle of attack are compared in Section III.C.

III.A. Smooth Case: $\alpha = 6°$

Before examining the effect of roughness elements, the growth and breakdown of second-mode waves on the smooth cone were measured. Several runs were conducted with unit Reynolds numbers from 3.5×10^6 /m

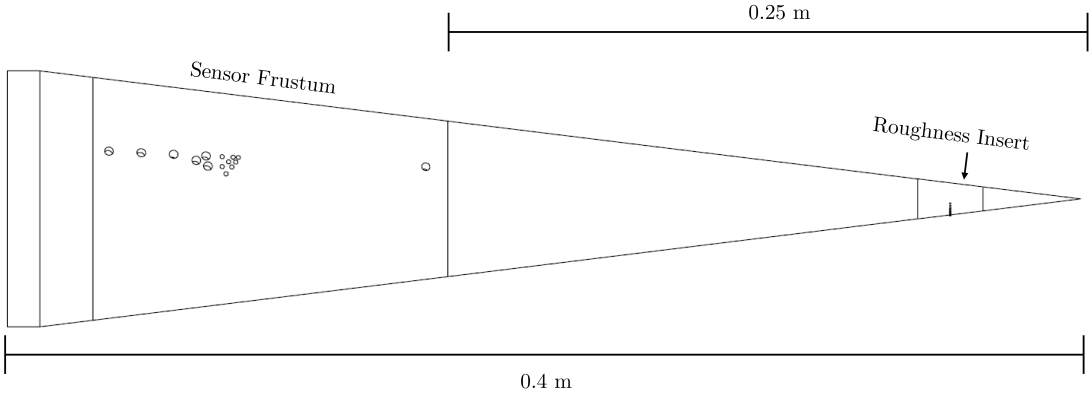

Figure 3. A schematic of the sensor frustum used in the present work.

to 17×10^6 /m. Figure 4(a) shows representative spectra from a few of these runs, illustrating the growth of the second-mode waves at around 200-300 kHz. No clear harmonics are evident for the highest amplitude cases, though the PSDs show some activity at frequencies near the expected first harmonic. The high-power peak at low frequencies below about 50 kHz is likely due to low-frequency tunnel noise.

Figure 4(b) shows the amplitude growth of the second mode with Reynolds number. The peak amplitude before breakdown is about 19%. Note that for this measurement location, $M_e \approx 5.5$. The measured peak amplitude compares well with the correlation provided by Marineau in Figure 7 of Reference 36 for second-mode growth on cones in hypersonic flow.

Color contours of surface temperature change from the pre-run condition, reduced from TSP images of the lee ray of the cone, are shown in Figure 5. Note the difference in scales: for higher Reynolds numbers, the boundary layer is thinner, resulting in higher heating. These images represent two different runs. For higher Reynolds numbers like in Figure 5(a), the boundary layer may be turbulent near the aft end of the model, as evident by the increase in temperature downstream. Stationary crossflow vortices are clearly visible as high-temperature streaks running roughly in the axial direction on both sides of the model. The lower heating at the lee ray is indicative of the mushroom-like bulge there, a result of the crossflow bringing fluid to the lee ray. See Reference 37 for computations illustrating this structure. At lower Reynolds numbers, like in Figure 5(b), stationary waves are less prominent due to the lower Reynolds number, but still visible especially on the right side of the model.

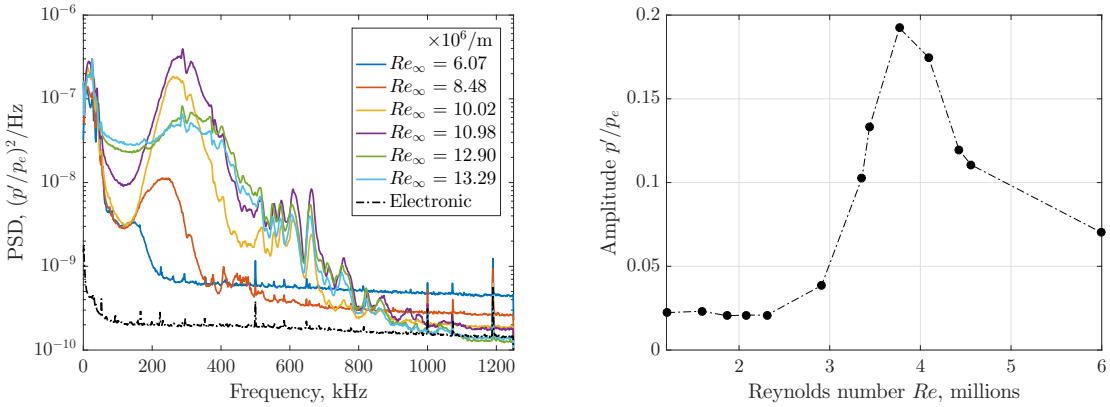

(a) Power spectral densities of the second-mode. The electronic spectrum is normalized by p_e for the $Re_\infty = 13.29 \times 10^6$ /m case.

(b) Amplitude growth.

Figure 4. The growth of the second-mode from laminar to turbulent at $M = 8$ and $\alpha = 6°$.

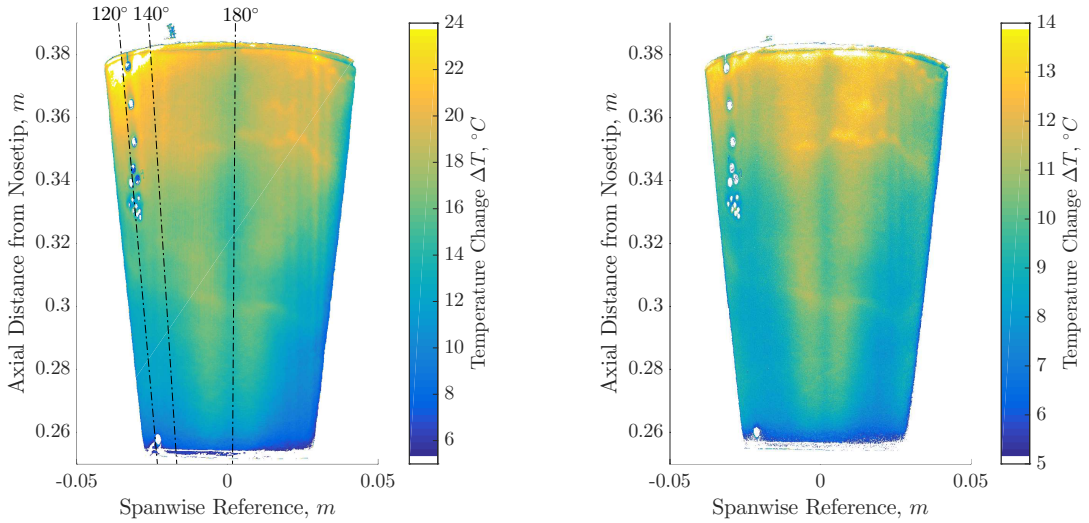

(a) $Re_\infty = 11.96 \times 10^6$ /m.

(b) $Re_\infty = 9.78 \times 10^6$ /m.

Figure 5. Temperature sensitive paint images of the lee side of the cone with smooth insert. Flow is from bottom to top. Note the change in temperature scale.

III.B. Effect of Roughness: $\alpha = 6°$

The addition of roughness patterns noticeably changes the results. Figure 6 shows TSP images comparing the cone's lee side for the smooth insert and the RIM 12x insert. Note that the unit Reynolds number for the roughness case is only about 65% of the smooth case. Streaks are evident in both images. For the roughness case, they appear only on the sensor side of the cone. Recall that the RIM 12x insert has roughness elements mostly on this side. Streak paths were extracted from the TSP in similar locations from both runs. The extracted paths are indicated as dots on each figure. To determine if the streaks in the roughness case were due to stationary waves (as opposed to roughness wakes), the streak paths are directly compared in Figure 7. Stationary crossflow vortices should approximately follow the inflection points in the boundary layer;[38] therefore if these streak paths are similar, then the streaks in the roughness case are likely due to stationary waves. From Figure 7, it is evident that the paths are quite similar. They are both slightly inclined from the edge streamline, as would be expected for stationary vortices. It therefore seems likely that the streaks measured using the roughness inserts are stationary crossflow vortices.

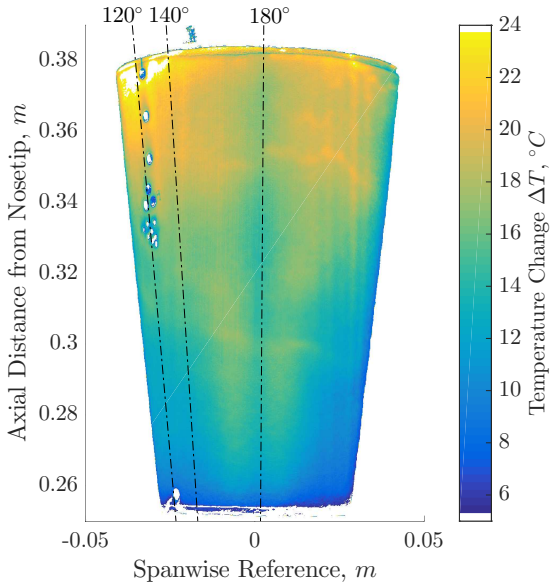

(a) Smooth case. $Re_\infty = 11.96 \times 10^6$ /m.

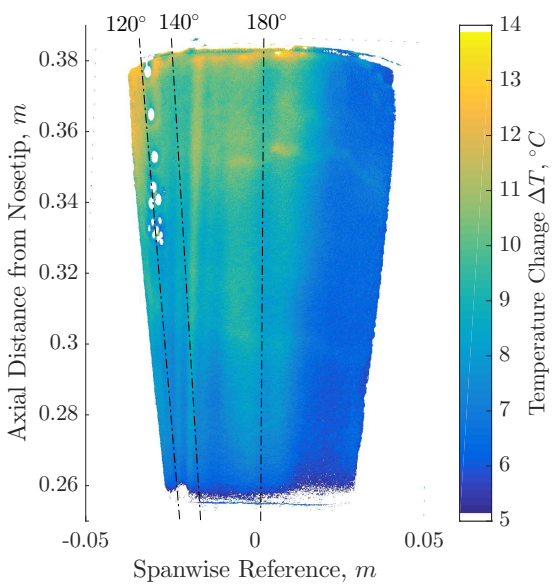

(b) RIM 12x roughness case. $Re_\infty = 7.74 \times 10^6$ /m.

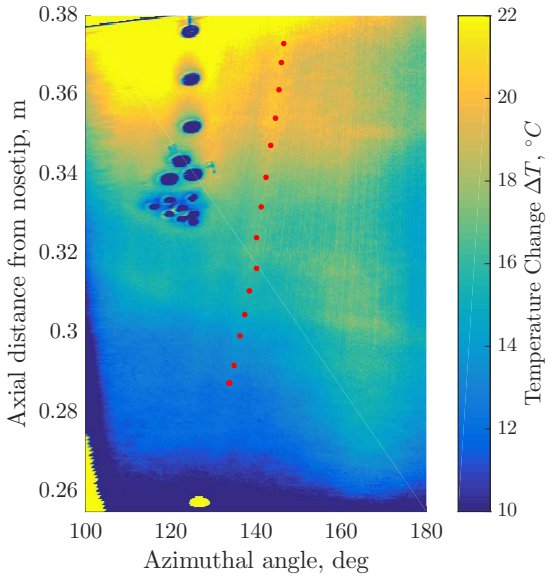

(c) Smooth case, unwrapped.

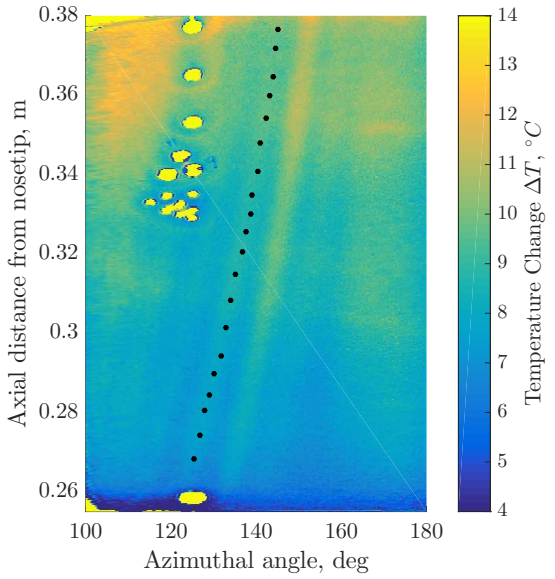

(d) RIM 12x case, unwrapped.

Figure 6. TSP images from runs with a smooth insert (a,c) and a roughness insert (b,d). The dots represent the visually extracted vortex paths. Note the different temperature scales.

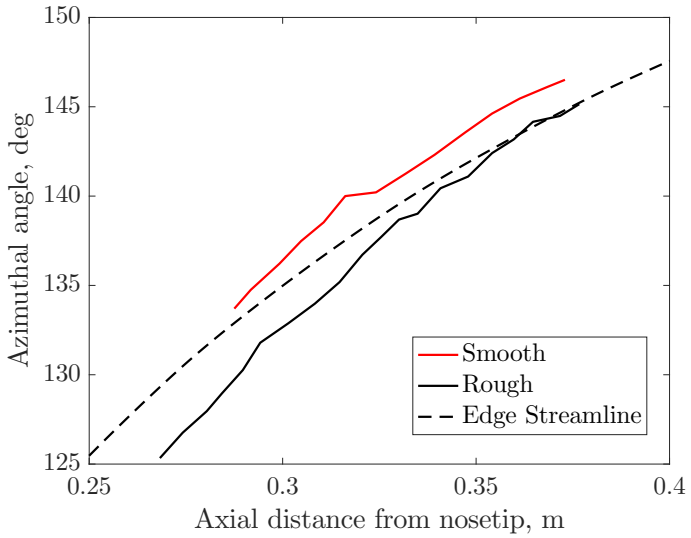

Figure 7. Comparison of vortex paths from the smooth and RIM 12x roughness cases.

The effect of added roughness is also apparent in the surface pressure measurements. Figure 8 shows PSDs from all three cases at similar Reynolds numbers. For both roughnesses, the spectra shows a large instability at about 225 kHz, one or two orders of magnitude larger than the smooth-cone second mode peak at about 150 kHz. The RIM 7x spectra shows spectral filling and appears to be near breakdown. The instability frequencies measured with the roughness are about 50% higher than the smooth-cone second-mode frequency. This could indicate that the roughness has generated a different instability, or it could be a consequence of the boundary layer distortion by the crossflow vortices. At Mach 6, there are modes of secondary instability of the stationary waves which appear like trapped second-mode waves, with frequencies altered by the changing boundary layer thickness.[12] Such a secondary instability could be important to stationary wave breakdown at Mach 8 as well, and would explain the change in the peak frequency.

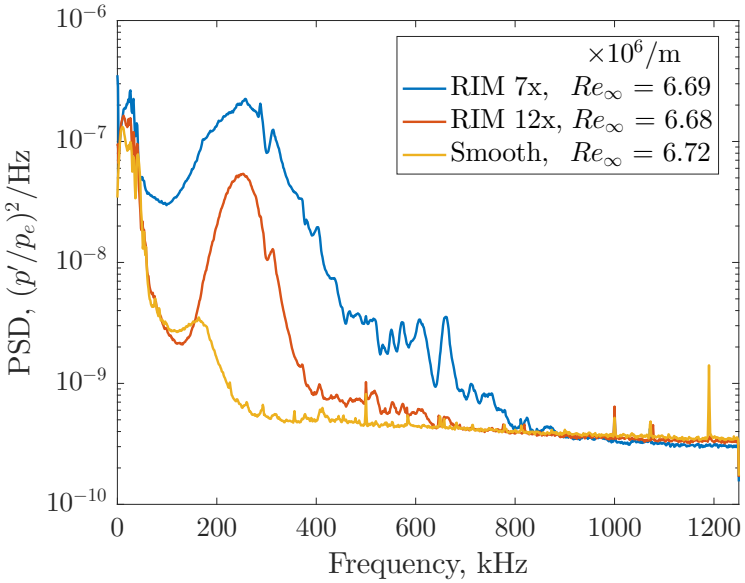

Figure 8. PSDs from runs with all three roughness inserts, at similar Reynolds numbers. $\alpha = 6°$.

The PSDs can be integrated to find the fluctuation amplitude of the instability normalized by the local edge pressure. The amplitude development with Reynolds number for each roughness case is shown in Figure 9. From Figure 9(a), it is evident that adding roughness results in earlier transition. For the RIM 12x

roughness, the peak amplitude is reached about 30% earlier than the smooth case, and about 40% earlier for the RIM 7x roughness. Interestingly, the peak amplitudes for the RIM 7x and smooth cases are about the same, approximately 18-19%, but the RIM 12x peak amplitude is much lower, about 14%. If these are in fact secondary instabilities of the stationary waves, then their amplitudes may be spanwise modulated,[13] so the peak amplitude is a function of the position of the sensor relative to the vortex. Thus since the two roughnesses produce different streak patterns owing to their different initial wavenumbers, this could explain the difference in peak amplitudes.

In addition to the shift of transition forward, roughness also appears to increase the growth rate of the instability from the smooth, second-mode case. This is better illustrated by Figure 9(b), which shows the logarithmic amplitude growth factors $\ln(A/A_0)$, where A_0 is the smallest measured amplitude (an approximation of the initial amplitude). In both cases with roughness, the slope of the initial growth of the instability is much higher than the smooth case. For both of these cases, the entire process from initial appearance of the instability to near turbulence takes about $Re = 2 \times 10^6$, whereas for the smooth case the process takes about $Re = 3.5 \times 10^6$.

That the RIM 7x roughness results in earlier transition than the RIM 12x roughness is interesting. It could be due to the fact that the RIM 7x roughness has 40% larger diameter roughness elements. It could also be due to the lower wavenumber. Forcing a wavenumber higher than the naturally amplified wavenumber can delay transition.[39] A future test will keep the roughness diameter constant and change the wavenumber to determine its effect.

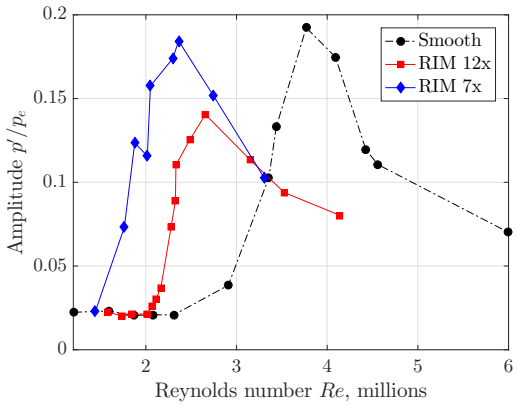

(a) Fluctuation amplitudes.

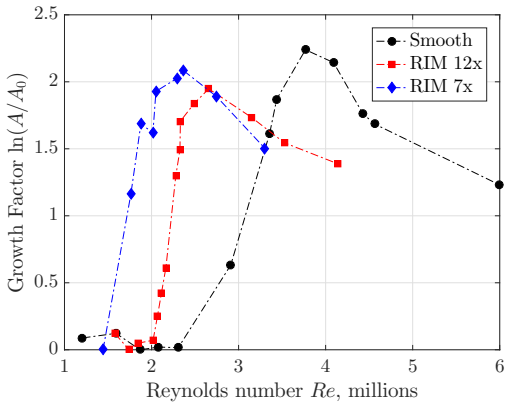

(b) Amplitude growth factors. A_0 is the smallest measured amplitude for each insert.

Figure 9. Amplitudes and amplitude growth factors for each roughness insert over nearly the entire development of the measured instabilities. $\alpha = 6°$.

The breakdown process of the vortices can be visualized in the TSP. Images of the side (90° ray) and the lee ray during a run using the RIM 7x roughness are shown in Figure 10. The 90° ray-side TSP image (Figure 10(a)) shows what appears to be crossflow waves breaking down near the sensors. Further leeward, the waves remain intact, though without pressure sensors it is difficult to judge the state of the boundary layer there. The corresponding PSDs of the two PCBs are provided in Figure 11. The spectral broadening in the PSDs show that at the PCB locations (~ 0.34 m) the boundary layer has begun to break down to turbulence. Note that this run is just before the peak amplitude in Figure 9(a) for the RIM 7x case.

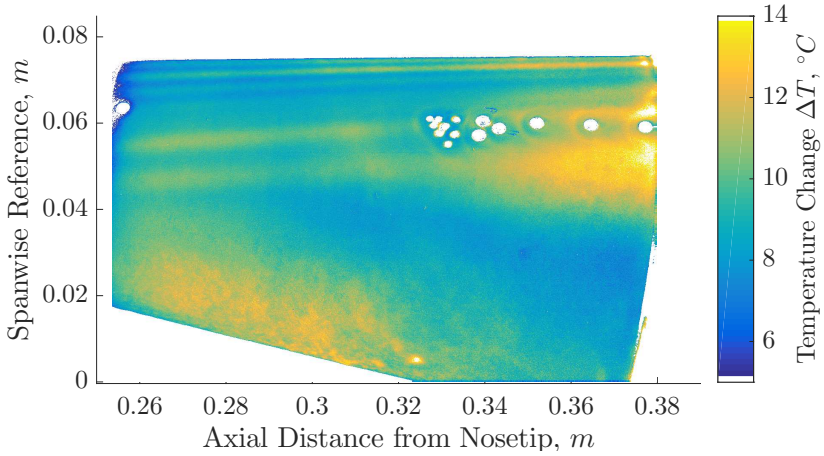

(a) 90° ray. Flow from left to right.

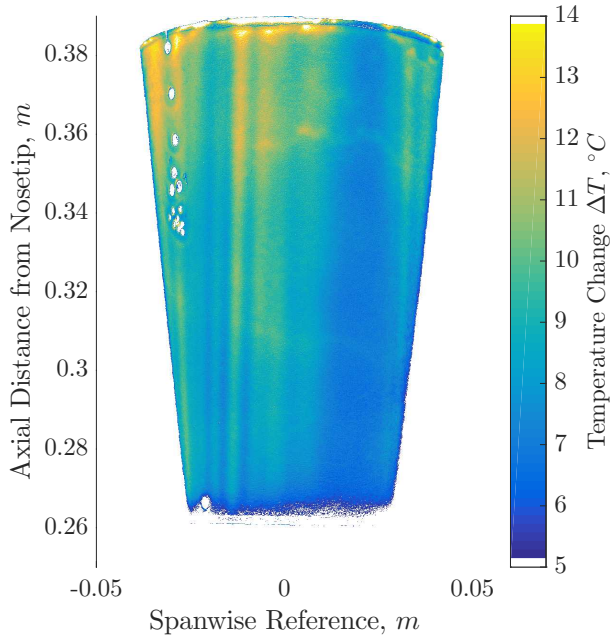

(b) Lee (180°) ray. Flow from bottom to top.

Figure 10. TSP images of the cone using the RIM 7x insert. $Re_\infty = 6.69 \times 10^6$ **/m.** $\alpha = 6^\circ$**.**

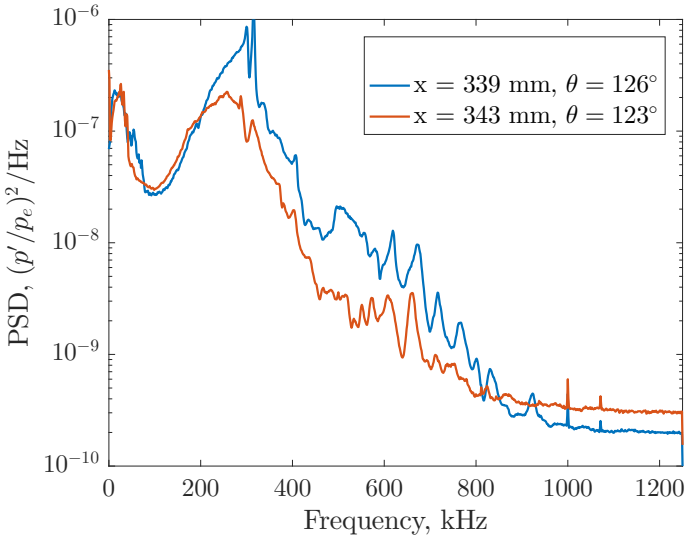

Figure 11. Power spectra at two PCB locations during the same run as Figure 10. $Re_\infty = 6.69 \times 10^6$ **/m.**

III.B.1. Effect of Rotation

At Mach 6 in quiet flow, there are large jumps in peak frequency of stationary wave secondary instabilities as a sensor is rotated leeward.[13] For instance, at Mach 6 the measured peak frequency changes from 160 kHz to 220 kHz as the sensor is rotated from 124° to 125°. A similar test was conducted in the present work, rotating the sensor frustum 10° leeward in steps of 2°. The resulting PSDs are shown in Figure 12. Note that the Reynolds numbers vary by less than 10% over the set of runs.

The measured instability does not have the same frequency pattern as secondary instabilities at Mach 6 in quiet flow. There is no jump in frequency; instead, the peak frequency smoothly decreases as the sensor is rotated leeward, a consequence of the monotonically thickening boundary layer. Some of the change in power over this set of runs can be explained by the variation in unit Reynolds number between runs. However, there appears to be an increase in amplitude as the sensor is rotated leeward; the 133° case is at lower Reynolds number than 127° and below, yet appears to have a higher amplitude. Data from the other sensor show the same trend. Figure 13 shows the measured peak frequencies as a function of azimuthal angle. As expected, with increasing azimuthal angle the peak frequency decreases, the result of increasing boundary layer thickness. However, at the highest angles measured, the peak frequency levels off. This behavior does not seem to correlate with differences in Reynolds number of wall temperature ratio between the runs.

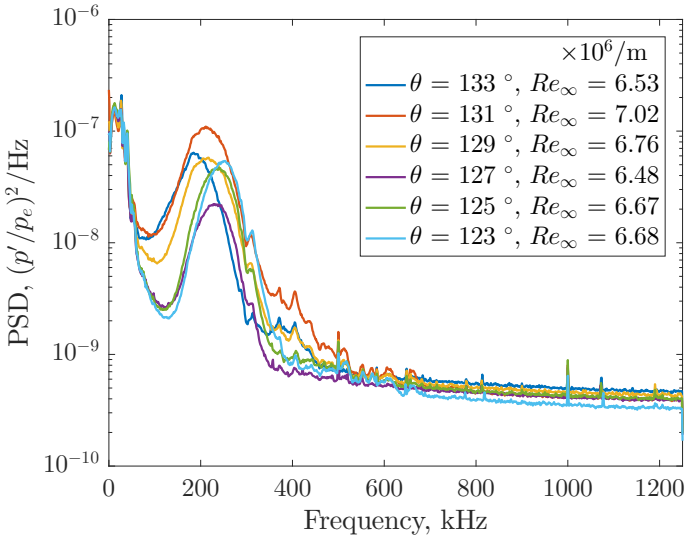

Figure 12. PSDs from $x = 343$ mm as the sensor is rotated leeward. RIM 12x roughness insert.

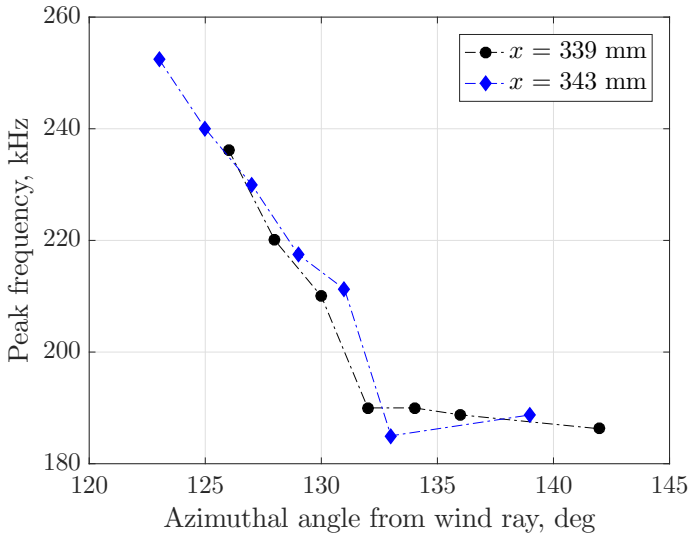

Figure 13. The measured peak frequencies from both sensors as azimuthal angle is increased. RIM 12x roughness insert. Same Reynolds numbers as Figure 12.

III.C. Effect of Angle of Attack

Figures 14 and 15 show the amplitudes and amplitude growth factors for each angle of attack (except 6°, provided in Figure 9) and for each roughness insert. The integration bands used to calculate the amplitudes are provided in Table 4. Note that for smaller angles of attack, the smallest measured amplitude (A_0) is higher for the roughness inserts than for the smooth case because a low enough Reynolds number was not achieved for these cases.

In general, for the smooth cone an increasing angle of attack delays transition onset, as visualized by the second-mode amplitudes. When roughness is added, increasing angle of attack promotes earlier transition than the equivalent smooth case. However, the peak amplitude with the RIM 12x roughness appears at approximately the same Reynolds number, regardless of angle of attack. The peak amplitudes of the measured instabilities, both with and without roughness, are all near 15-20%. This is equivalent to a logarithmic growth factor of 1.5-2.

The roughness inserts have no elements leeward of the 90° ray, so at small angles of attack the results

should be the same as with the smooth insert because the stationary vortex paths from the roughness elements will not curve enough to reach the sensors. Figures 14(a-b) and 15(a-b) illustrate this effect at 0° and 2° angle of attack. The amplitude curves for each roughness lie on top of the smooth case for both angles, and the growth rates are similar.

Between 2° and 4°, noticeable differences develop between the three cases. At 4° angle of attack (Figures 14(c) and 15(c)), both roughness inserts cause early transition, though the RIM 7x insert destabilizes the boundary layer more than the RIM 12x insert, as was the case at 6° angle of attack. For the 4°, the peak amplitudes for each roughness are about the same, but both are 20% lower than the smooth case peak amplitude.

At 8° (Figures 14(d) and 15(d)), the RIM 12x roughness causes the earliest transition, unlike in the 4° and 6° cases. The reason for this switch is unclear. Here all the peak amplitudes are about the same. It appears that the measurements did not capture the true peak amplitude of the RIM-7x case, which is likely around $Re = 3 \times 10^6$. In addition, unlike in the other cases the growth rate of the RIM 12x case seems to be slightly higher than the RIM 7x case (see Figure 15(d)). Note that computations are needed to better understand the behavior of the growth rates for all the measured cases.

In all the cases, the RIM 12x roughness reaches the same peak amplitude. The smooth case peak amplitude initially increases from 0°, but drops by about 30% between 6° and 8°.

The difference between the streak paths at 4°, 6°, and 8° angle of attack is illustrated in Figure 16. In general, the streak paths become more sharply angled to the lee ray at higher angles of attack, a result of larger pressure gradients. Note that at 6° and 8° in Figure 16(c), there are streaks on both sides of the model. This is likely due to the two roughness elements on the non-sensor-side at 9° and 27° from the wind ray. As the vortex paths become steeper, they appear closer to the lee ray on the image.

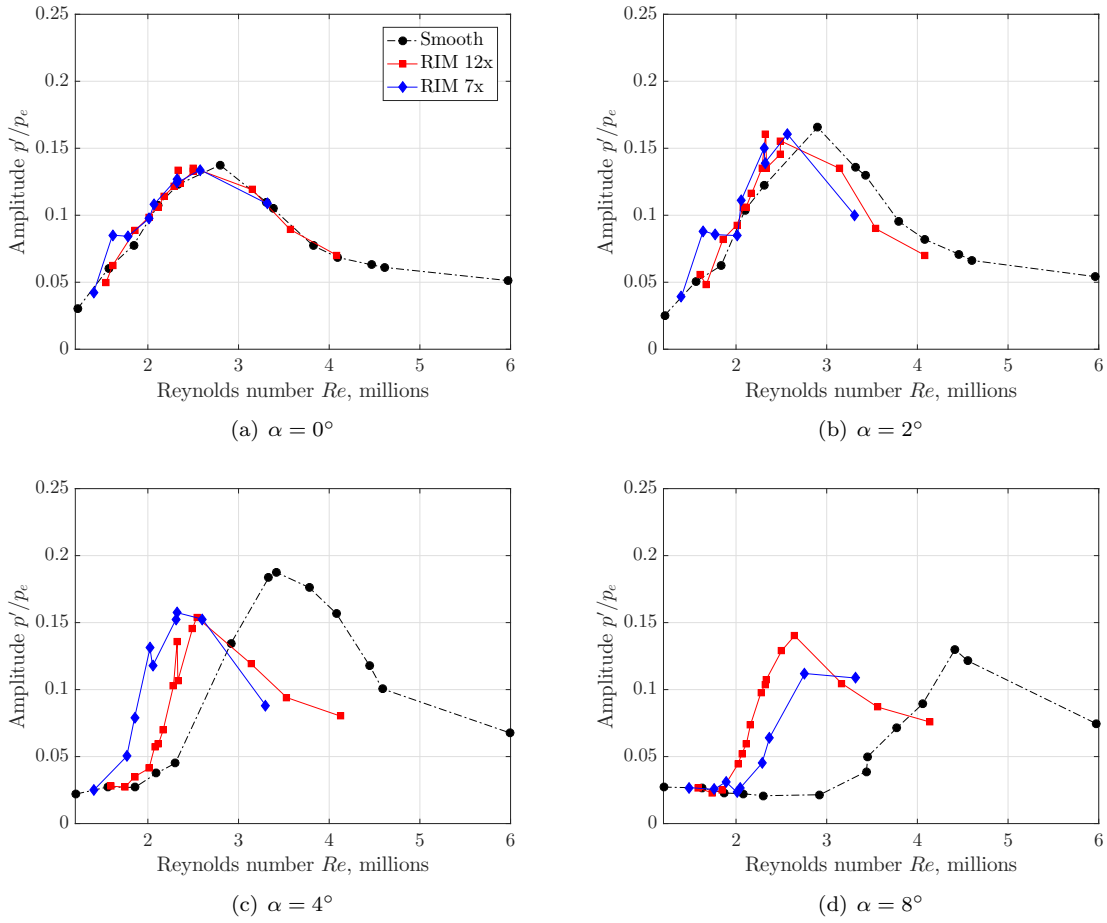

Figure 14. Amplitudes for each roughness insert at each angle of attack.

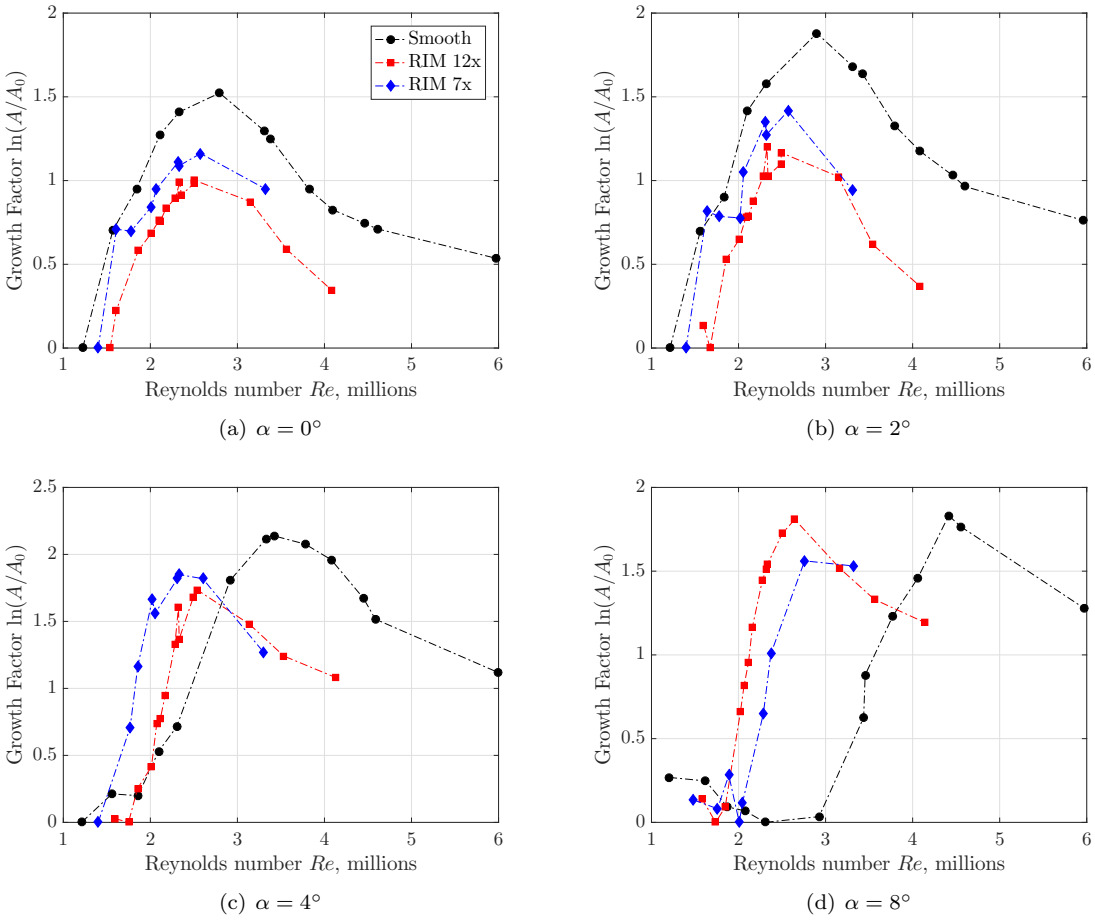

Figure 15. Amplitude growth factors for each roughness insert at each angle of attack.

Table 4. Frequency integration bands for calculating amplitudes at each angle of attack.

α, deg.	integration band, kHz
0	[90, 300]
2	[90, 300]
4	[90, 500]
6	[110, 500]
8	[110, 500]

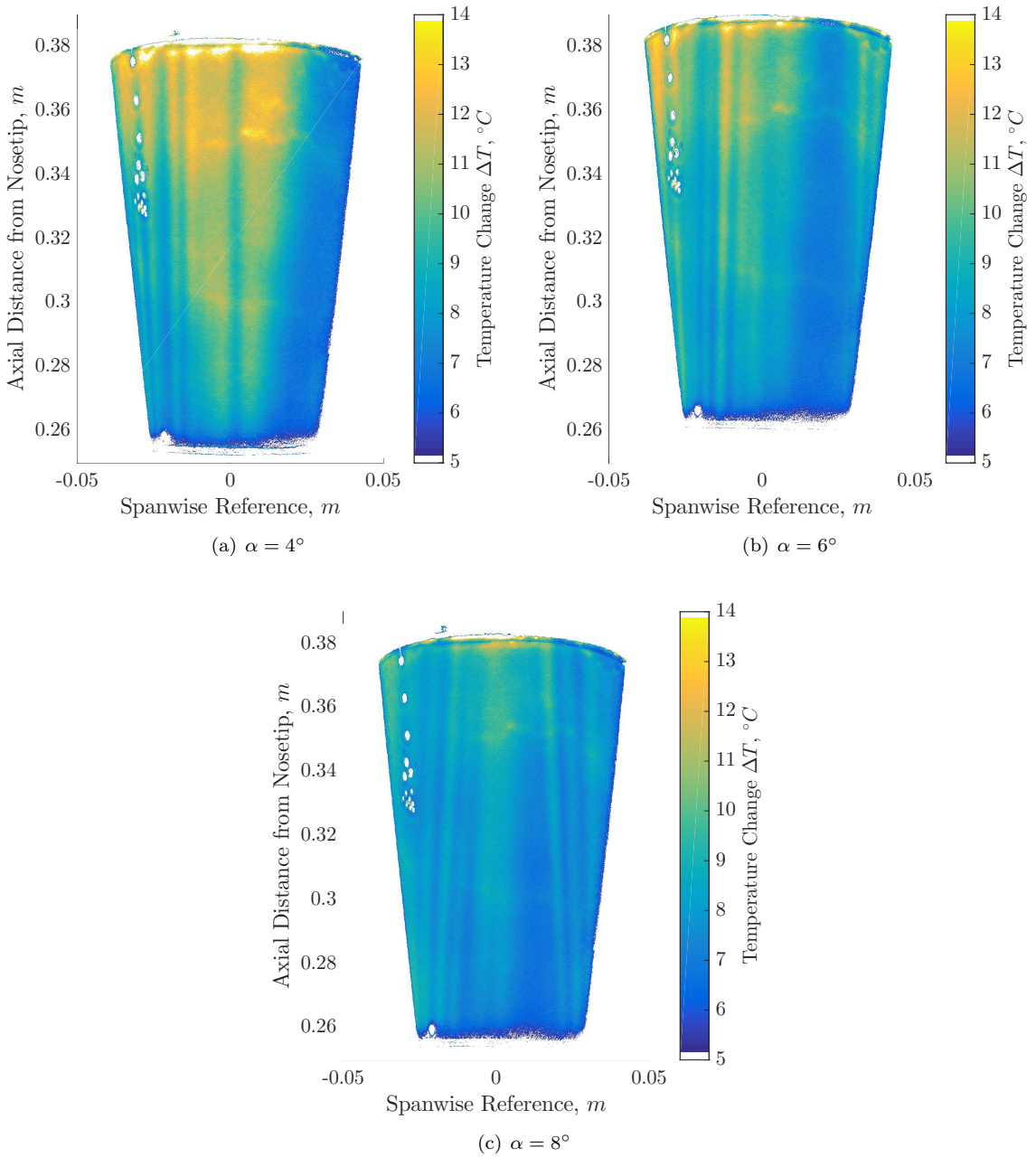

(a) $\alpha = 4^\circ$

(b) $\alpha = 6^\circ$

(c) $\alpha = 8^\circ$

Figure 16. TSP images of the lee ray of the cone at three angles of attack. RIM 7x insert. Flow is from bottom to top.

III.D. Comparison to Purdue Data

The Modular Cone was also tested in the Boeing/AFOSR Mach-6 Quiet Tunnel (BAM6QT) at Purdue University. The BAM6QT can be run in 'noisy' mode, with freestream noise levels comparable to other conventional tunnels. For this test, a different Sensor Insert was used in the cone, but there were PCBs located at similar positions on both inserts. For the BAM6QT data, data was taken at $x = 341$ mm from the nosetip. Both sets of data were taken at 123° from the wind ray. Other than the Sensor Insert, the Modular Cone hardware was the same for both tests. The BAM6QT data is only at 6° angle of attack.

Figure 17 shows the measured instability amplitudes in the 110 - 500 kHz band for both sets of data at 6° angle of attack. Data is shown from runs using the smooth roughness insert and the RIM12x-5 roughness insert. The Reynolds number based on sensor axial position has been normalized by the nominal freestream Mach number (8 for the HWT-8 and 6 for the BAM6QT). The fluctuation amplitudes are normalized by

the freestream Mach number squared. Using this scaling, the amplitude development with the RIM12x-5 roughness matches closely between the two tunnels. The second-mode development with the smooth insert is only close in the initial, linear portion. The peak is much smaller for the BAM6QT smooth data than for HWT-8.

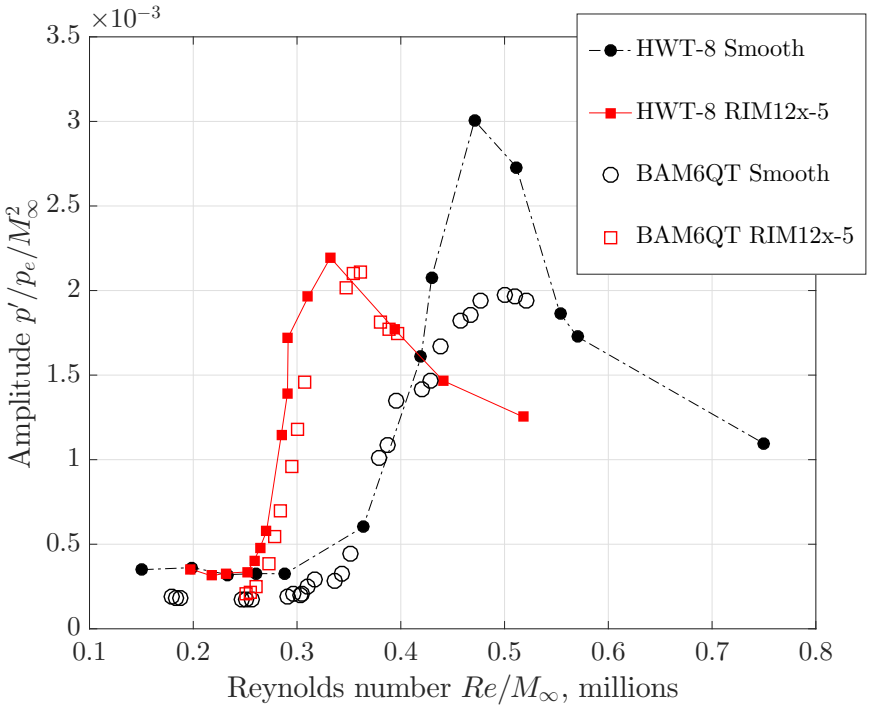

Figure 17. Comparison of measured instability amplitudes in the Sandia HWT-8 (Mach 8) and the Purdue BAM6QT (Mach 6). The amplitudes are calculated in the 110 - 500 kHz band.

IV. Travelling Crossflow Results

An array of closely-spaced Kulite pressure sensors was used to attempt to measure travelling crossflow wave growth, speed, and propagation angle. Figure 18(a) shows the placement of these Kulites. A positive value on the y-axis indicates the Kulite is closer to the wind ray. Following the procedure outlined by Poggie et al.[26] (also used by Borg et al.[3] and Ward[29]), the phase speed c_r and propagation angle Ψ of the travelling waves can be calculated. Note that for the present work a positive propagation angle is oriented downstream and toward the windward ray as illustrated in Figure 18(b).

IV.A. Effect of Angle of Attack

A low-frequency, coherent wave was measured at all five angles of attack. Figure 19(a) shows the power spectra of Kulite 1 at $x = 328$ mm for each angle of attack. The Reynolds number was within 0.1×10^6 /m of $Re_\infty = 6.7 \times 10^6$ /m for all the angles of attack. The narrow peak at about 275 kHz is the Kulite resonance, and the wider peak from about 150 - 300 kHz is the second-mode (or secondary instability), which is evidently highly dependent on the angle of attack. The strong, sharp peak at around 275 kHz is the resonance of the Kulite sensor. Data from above 10-20% of the resonance frequency should be considered illustrative but not necessary accurate.

The low-frequency wave is present at about 5-10 kHz. The amplitude in the low-frequency band does not change much with angle of attack. The coherence between Kulites 1 and 2 ($x = 330$ mm) is provided in Figure 19(b). There is a large coherence in the low frequency band (as well as the second-mode band) for all angles of attack.

The wave properties were calculated from Kulites 1, 2, and 4 (2.75° windward, and $x = 329$ mm). The propagation angle and the phase speed of the waves are shown for each angle of attack in Figure 20.

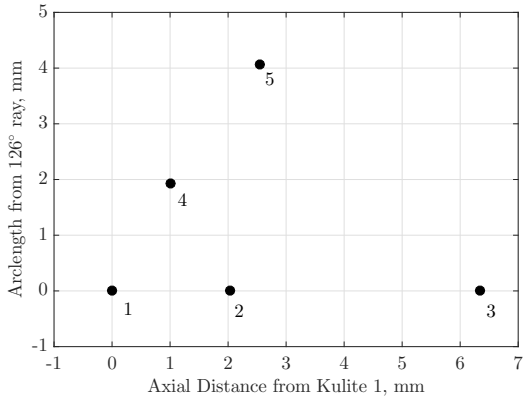

(a) Location of the Kulite sensors used to measure travelling wave properties.

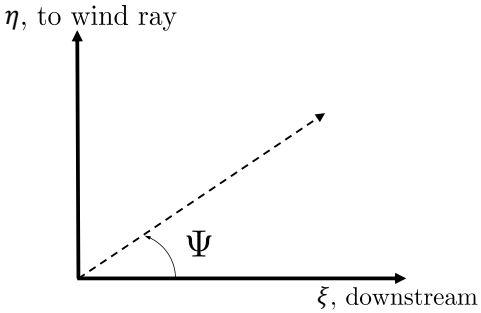

(b) The orientation of the wave angle coordinate system with respect to the cone model.

Figure 18. Kulite sensor array properties.

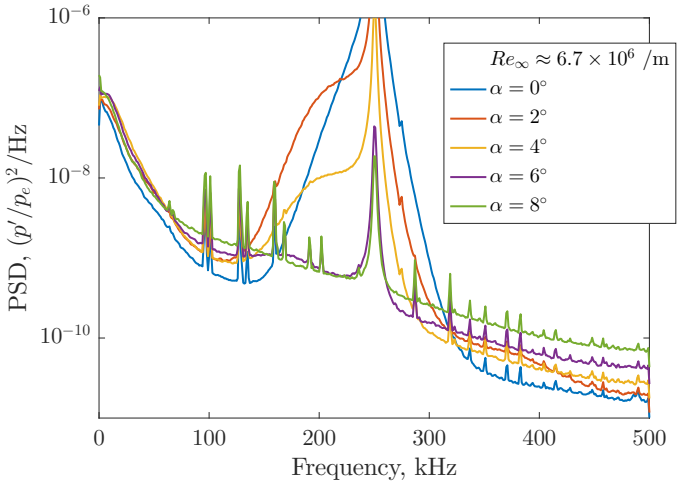

(a) Power spectra.

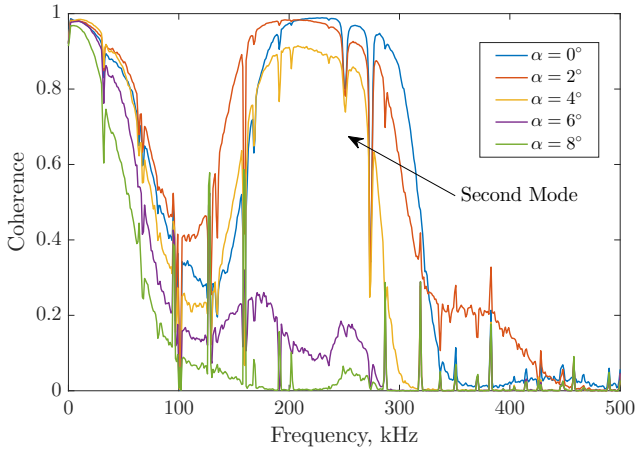

(b) Coherences.

Figure 19. Spectra of the Kulite measurements.

The propagation angles are fairly similar for the non-zero angles of attack, decreasing roughly linearly with increasing frequency. The propagation angle for $\alpha = 0°$ is well below the others, with a much steeper decline at low frequencies. In all cases, the propagation angle is positive. This means that the waves are travelling downstream and toward the wind ray. In the case of 0° there is nominally no wind ray, but it is likely that the cone was instead at a small, non-zero angle of attack.

The phase velocities vary more dramatically between angles of attack. At angles above $\alpha = 4°$, the calculated velocities are very similar. At $\alpha = 2°$, the low-frequency velocity has increased by almost 100%, and at $\alpha = 0°$, the phase velocity is near the edge velocity for all frequencies.

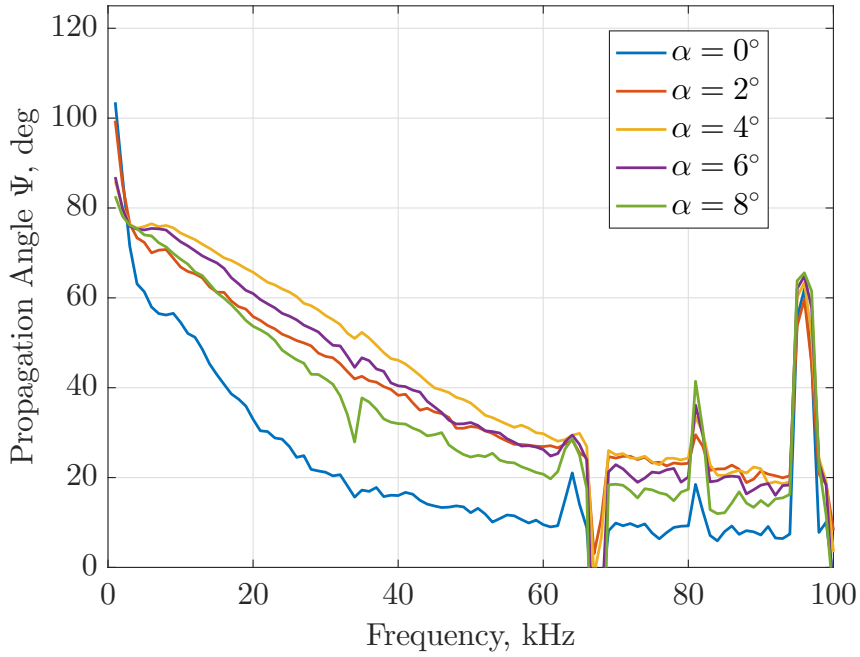

(a) Propagation angle Ψ.

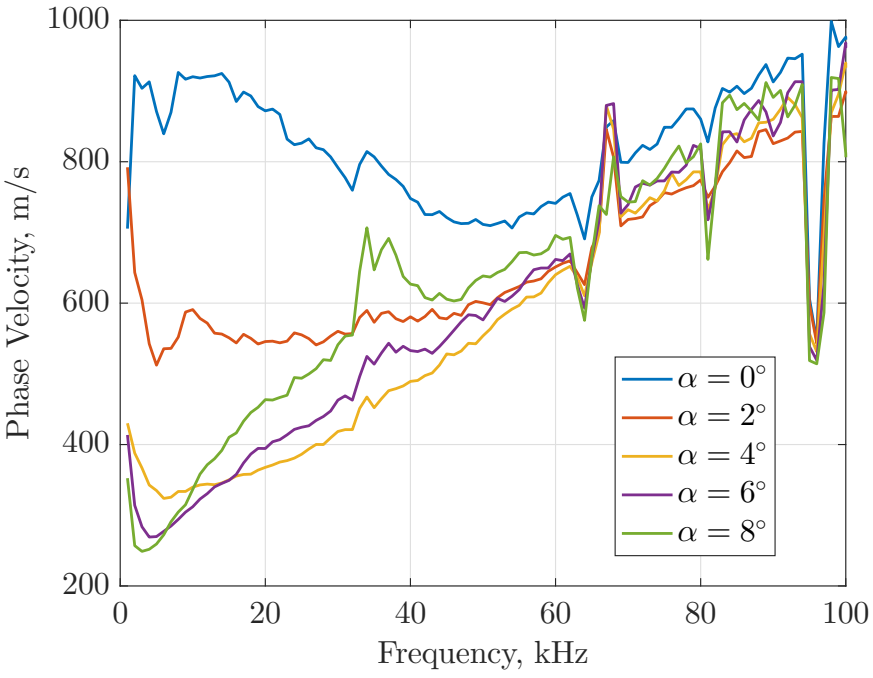

(b) Phase speed c_r.

Figure 20. Wave properties for the low-frequency waves at each angle of attack.

IV.B. Comparison to Computations and Elliptical Cone Data

The measured wave properties can be compared to stability computations and to measurements on an elliptical cone by Borg, et al.[4] in the Purdue BAM6QT (under noisy flow conditions) and the Texas A&M ACE. The comparisons are provided in Figure 21. The HWT-8 data is for the smooth cone at 6° angle of

attack.

The computations clearly do not match the measured properties. The computed travelling wave propagation angle decreases much more slowly with frequency than the measurement, and the computed wave speed is about double the measured wave speed for most frequencies.

However, the measured wave properties in HWT-8 are quite similar to the measurements made by Borg, et al. It is unclear why this might be the case, as the measurements were made in different tunnels on different geometries at different Mach numbers. It is possible that all the low-frequency measurements are a tunnel-noise-driven instability. Further experiments and computations are necessary to better understand these measurements.

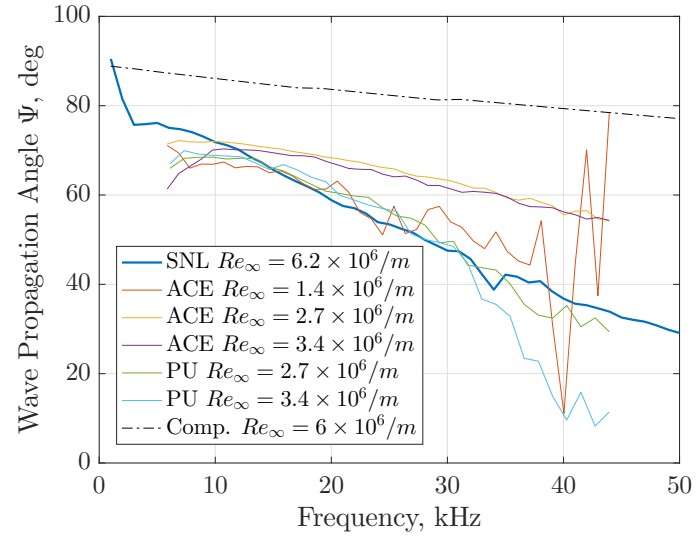

(a) Wave propagation angle.

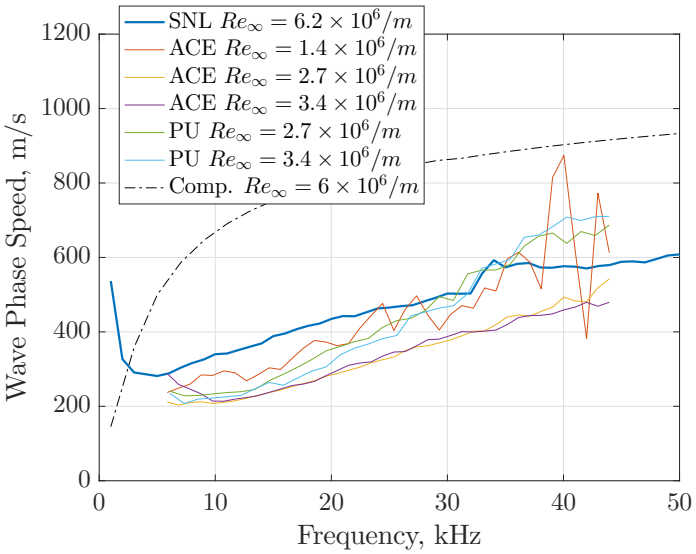

(b) Wave phase speed.

Figure 21. Measurements of low-frequency wave properties from HWT-8, Purdue University BAM6QT, and Texas A&M ACE, as well as computations.

V. Discussion and Conclusions

V.A. Stationary Crossflow

Two patterns of roughness elements were placed near the nosetip of a pitched 7° half-angle cone at Mach 8 to excite stationary crossflow waves. The goal of this experiment was to force stationary crossflow waves as the dominant transition mechanism in a noisy environment, instead of the second mode. Once stationary crossflow waves were excited at high enough amplitudes, their breakdown could be measured using fast surface-pressure sensors and temperature sensitive paint.

The roughness elements generated streaks in TSP images of the cone. Because the Re_k of the roughness is very low and the roughness-excited streaks follow the same path as naturally-excited stationary crossflow waves on the smooth cone, it is believed that the roughness elements are generating stationary crossflow waves. This technique has been used with success in quiet tunnels.[13]

The addition of roughness appears to destabilize the boundary layer. Boundary-layer transition occurs between 30% and 40% sooner with the addition of roughness at $\alpha = 6°$. In addition, the growth rate of the measured instability caused by the roughness is much higher than the growth rate of the second-mode on a smooth cone. Transition from initial appearance of the instability in laminar flow to near turbulence takes only about $Re = 1.5 - 2 \times 10^6$. Using larger diameter roughness elements at a wavenumber of 20 results in earlier transition than for a wavenumber of 40, except at $\alpha = 8°$.

TSP images appear to show the stationary vortices breaking down near the surface pressure sensors. These images, in addition to the explosive growth of the roughness-generated instabilities and the sensitivity to roughness parameters suggest that stationary crossflow wave breakdown is being observed, and the measured instabilities could be secondary instabilities of these waves. However, unlike measurements of secondary instabilities at Mach 6 in quiet flow, there does not appear to be a change in instability mode with changing azimuthal angle. Future work will include comparison to computations to better understand the nature of stationary crossflow secondary instabilities in this flow, and the effect of periodic roughness elements. In addition, future experiments will perform similar measurements at Mach 5, and with various additional roughness heights and spacings. It appears that using the RIM-type roughness elements, stationary crossflow wave breakdown can be studied in conventional tunnels. However, comparisons to quiet tunnel data are needed to develop a transition prediction criterion using this noisy tunnel data.

V.B. Travelling Crossflow

A closely-spaced array of pressure sensors allowed the calculation of wave speeds and propagation angles of a low-frequency instability on the pitched cone. Very high coherences indicate that the measurements are not spurious. For all non-zero angles of attack, the propagation angle of the measured low-frequency instability is in the expected direction for travelling waves, namely downstream and toward the wind ray.

The phase velocity of the low-frequency waves varies considerably with the different angles of attack, from the edge velocity at 0° down to only about 200 m/s at 8°. In addition, the measured phase velocity is well below the computation. However, the measured phase velocity is close to those measured by Borg, et al. in the Purdue BAM6QT and the Texas A&M ACE tunnels on an elliptic cone.

There is no reason to expect that travelling crossflow waves would behave similarly on these different geometries, though it is possible that they might. Another intriguing possibility is that the measured low-frequency wave may in fact be an instability driven by tunnel noise, comparable to those of Borg, et al., rather than the travelling crossflow instability.

Acknowledgments

The authors would like to thank Dr. Neal Bitter for providing multiple US3D CFD solutions. Thanks are also due to Dr. Steve Beresh and Dr. Ed DeMauro for their help in setting up the TSP camera hardware and software. We are grateful for the elliptical cone data provided by Dr. Matthew Borg. Finally, thanks to Jerry Hahn, Robin Snodgrass, and Jim Younts of the Purdue AAE Machine Shop for their help in designing and manufacturing the model hardware.

Funding for the model was provided by the Air Force Office of Scientific Research under grant number FA9550-12-1-0167.

This work is supported by Sandia National Laboratories and the United States Department of Energy.

Sandia National Laboratories is a multi-program laboratory managed and operated by the Sandia Corporation, a wholly owned subsidiary of the Lockheed Martin Corporation, for the U.S. Department of Energy's National Nuclear Security Administration, under contract DE-AC04-94AL85000.

References

[1]Saric, W. S., Reed, H. L., and White, E. B., "Stability and Transition of Three-Dimensional Boundary Layers," *Annual Review of Fluid Mechanics*, Vol. 35, 2003, pp. 413–440.

[2]Deyhle, H. and Bippes, H., "Disturbance Growth in an Unstable Three-Dimensional Boundary Layer and Its Dependence on Environmental Conditions," *Journal of Fluid Mechanics*, Vol. 316, 1996, pp. 73–113.

[3]Borg, M. P., Kimmel, R. L., and Stanfield, S., "Traveling Crossflow Instability for the HIFiRE-5 Elliptic Cone," *Journal of Spacecraft and Rockets*, Vol. 52, No. 3, May-June 2015.

[4]Borg, M., Kimmel, R., Hofferth, J., Bowersox, R., and Mai, C., "Freestream Effects on Boundary Layer Disturbances for HIFiRE-5," *AIAA 2015-0278*, January 2015.

[5]Bippes, H., "Basic Experiments on Transition in Three-Dimensional Boundary Layers Dominated by Crossflow Instability," *Progress in Aerospace Sciences*, Vol. 35, No. 4, May 1999, pp. 363–412.

[6]Kohama, Y., Saric, W., and Hoos, J., "A High-Frequency, Secondary Instability of Crossflow Vortices that Leads to Transition," *Proceedings of the Conference on Boundary Layer Transition and Control*, 1991, pp. 4.1–4.13.

[7]Malik, M., Li, F., and Chang, C.-L., "Nonlinear Crossflow Disturbances and Secondary Instabilities in Swept-Wing Boundary Layers," *IUTAM Symposium on Nonlinear Instability and Transition in Three-Dimensional Boundary Layers*, edited by P. W. Duck and P. Hall, 1996, pp. 257–266.

[8]Malik, M., Li, F., Choudhari, M., and Chang, C.-L., "Secondary Instability of Crossflow Vortices and Swept-Wing Boundary-Layer Transition," *Journal of Fluid Mechanics*, Vol. 399, 1999, pp. 85–115.

[9]White, E. and Saric, W., "Secondary Instability of Crossflow Vortices," *Journal of Fluid Mechanics*, Vol. 525, 2005, pp. 275–308.

[10]Craig, S. and Saric, W., "Experimental Study of Crossflow Instability on a Mach 6 Yawed Cone," *AIAA 2015-2774*, June 2015.

[11]Ward, C., Henderson, R., and Schneider, S., "Possible Secondary Instability of Stationary Crossflow Vortices on an Inclined Cone at Mach 6," *AIAA 2015-2773*, June 2015.

[12]Moyes, A., Paredes, P., Kocian, T., and Reed, H., "Secondary Instability Analysis of Crossflow on a Hypersonic Yawed Straight Circular Cone," *AIAA 2016-0848*, January 2016.

[13]Edelman, J. B., Chynoweth, B. C., McKiernan, G. R., Sweeney, C. J., and Schneider, S. P., "Instability Measurements in the Boeing/AFOSR Mach-6 Quiet Tunnel," *AIAA 2016-3343*, June 2016.

[14]Schneider, S., "Hypersonic Laminar-Turbulent Transition on Circular Cones and Scramjet Forebodies," *Progress in Aerospace Sciences*, Vol. 40, No. 1-2, February 2004, pp. 1–50.

[15]Muñoz, F., Heitmann, D., and Radespiel, R., "Instability Modes in Boundary Layers of an Inclined Cone at Mach 6," *Journal of Spacecraft and Rockets*, Vol. 51, No. 2, March-April 2014.

[16]van den Kroonenberg, A., Radespiel, R., Candler, G., and Estorf, M., "Infrared Measurements of Boundary-Layer Transition on an Inclined Cone at Mach 6," *AIAA 2010-1063*, January 2010.

[17]Swanson, E. and Schneider, S., "Boundary-Layer Transition on Cones at Angle of Attack in a Mach-6 Quiet Tunnel," *AIAA 2010-1062*, January 2010.

[18]Li, F., Choudhari, M. M., and Duan, L., "Direct Numerical Simulation of Transition due to Traveling Crossflow Vortices," *AIAA 2015-2771*, June 2015.

[19]Malik, M. R., Li, F., and Chang, C.-L., "Crossflow Disturbances in Three-Dimensional Boundary Layers: Nonlinear Development, Wave Interaction and Secondary Instability," *Journal of Fluid Mechanics*, 1994, pp. 1–36.

[20]Wassermann, P. and Kloker, M., "Transition Mechanisms Induced by Travelling Crossflow Vortices in a Three-Dimensional Boundary Layer," *Journal of Fluid Mechanics*, Vol. 483, 2003, pp. 67–89.

[21]Bonfigli, G. and Kloker, M., "Secondary Instability of Crossflow Vortices: Validation of the Stability Theory by Direct Numerical Simulation," *Journal of Fluid Mechanics*, Vol. 583, 2007, pp. 229–272.

[22]Li, F., Choudhari, M. M., Duan, L., and Chang, C.-L., "Nonlinear Development and Secondary Instability of Traveling Crossflow Vortices," *AIAA 2014-1132*, January 2014.

[23]Li, F., Choudhari, M., Chang, C.-L., White, J., Kimmel, R., Adamczak, D., Borg, M., Stanfield, S., and Smith, M., "Stability Analysis for HIFiRE Experiments," *AIAA 2012-2961*, June 2012.

[24]T. Lerche, "Experimental Investigation of Nonlinear Wave Interactions and Secondary Instability in Three-Dimensional Boundary-Layer Flow," *Proceedings of the 6th European Turbulence Conference, Advances in Turbulence VI*, 1996, pp. 357–360.

[25]Eppink, J. and Wlezien, R., "Observations of Traveling Crossflow Resonant Triad Interactions on a Swept Wing," *AIAA 2012-2820*, June 2012.

[26]Poggie, J., Kimmel, R. L., and Schwoerke, S. N., "Traveling Instability Waves in a Mach 8 Flow over an Elliptic Cone," *AIAA Journal*, Vol. 38, No. 2, February 2000, pp. 251–258.

[27]Borg, M. P., Kimmel, R. L., and Stanfield, S., "Traveling Crossflow Instability for HIFiRE-5 in a Quiet Hypersonic Wind Tunnel," *AIAA 2013-2737*, June 2013.

[28]Muñoz, F., Radespiel, R., Theiss, A., and Hein, S., "Experimental and Numerical Investigation of Instabilities in Conical Boundary Layers at Mach 6," *AIAA 2014-2778*, June 2014.

[29]Ward, C., *Crossflow Instability and Transition on a Circular Cone at Angle of Attack in a Mach-6 Quiet Tunnel*, Ph.D. thesis, Purdue University, December 2014.

[30]Casper, K., *Hypersonic Wind-Tunnel Measurements of Boundary-Layer Pressure Fluctuations*, Master's thesis, Purdue University, August 2009.

[31]Sweeney, C., Chynoweth, B., Edelman, J., and Schneider, S., "Instability and Transition Experiments in the Boeing/AFOSR Mach 6 Quiet Tunnel," *AIAA 2016-0355*, January 2016.

[32]Chynoweth, B., *A New Roughness Array for Controlling the Nonlinear Breakdown of Second-Mode Waves at Mach 6*, Master's thesis, Purdue University, August 2015.

[33]Schneider, S., "Effects of Roughness on Hypersonic Boundary-Layer Transition," *Journal of Spacecraft and Rockets*, Vol. 45, No. 2, March-April 2008.

[34]Braslow, A. L., "A Review of Factors Affecting Boundary-Layer Transition," Tech. rep., NASA TN D-3384, August 1966.

[35]PCB Piezotronics, *ICP Pressure Sensor 132A31 Datasheet*, October 2015, Rev. R.

[36]Marineau, E. C., "Prediction Methodology for Second-Mode-Dominated Boundary-Layer Transition in Wind Tunnels," *AIAA Journal*, Vol. 55, No. 2, February 2017.

[37]Li, F., Choudhari, M. M., Chang, C.-L., and White, J., "Analysis of Instabilities in Non-Axisymmetric Hypersonic Boundary Layers over Cones," *AIAA 2010-4643*, July 2010.

[38]Oliviero, N., Kocian, T., Moyes, A., and Reed, H., "EPIC: NPSE Analysis of Hypersonic Crossflow Instability on Yawed Straight Circular Cone," *AIAA 2015-2772*, June 2015.

[39]Schuele, C., Corke, T., and Matlis, E., "Control of Stationary Cross-flow Modes in a Mach 3.5 Boundary Layer Using Patterned Passive and Active Roughness," *Journal of Fluid Mechanics*, Vol. 718, 2013, pp. 5–38.